ORIGINAL PAPER

Visible light photodegradation of blue basic 41 using cobalt doped ZnO: Box–Behnken optimization and DFT calculation

Karim Tanji[1] · Morad Zouheir[1] · Yassine Naciri[2] · Hassan Ahmoum[3] · Abdelghani Hsini[2] · Oumaima Mertah[1] · Abdelali El Gaidoumi[5] · J. A. Navio[4] · M. C. Hidalgo[4] · Abdelhak Kherbeche[1]

Abstract

$Co_xZn_{1-x}O$ system ($0 \leq x \leq 0.2$) was synthesized using the solution combustion method with urea as a fuel source. Photocatalytic tests were performed under visible light to assess the Basic Blue 41 (BB41) conversion. Various characterization techniques, including XRD, FT-IR analysis, SEM, EDS, XRF, BET-surface area, and DRS were used to investigate the composition, structure, and morphology of the synthesized catalysts. In addition, the density functional theory calculation was used in order to study the electronic properties of the ZnO structure. The Box–Behnken model was valid for describing the degradation of BB41 dye according to the analysis of variances results. A maximum conversion of 100% for BB41 dye has been reached with high mineralization and important removal of chemical oxygen demand. The optimum conditions for BB41 conversion are reported. On the other hand, the reuse tests of the best catalyst showed high-performance stability after five cycles. Furthermore, the activity of superoxide ions ($O_2^{\cdot-}$) and hydroxyl radicals ($OH^{\cdot}$) as the spices responsible for BB41 dye conversion was well confirmed by the free radicals scavenging tests. The use of Box–Behnken optimization and DFT calculation applied to the synthesized catalysts proves to be a very suitable procedure to establish the operating conditions under which the synthesis strategy of the $Co_xZn_{1-x}O$ catalyst in its activity in the visible region performs an excellent efficiency for the degradation of organic dyes and makes contributions to the current literature related to the field of environmental technology.

Keywords Visible light · Cobalt doped ZnO · Basic blue 41 · Box · Behnken design · DFT

✉ Karim Tanji
   karim.tanji@usmba.ac.ma

✉ Yassine Naciri
   yassine.naciri@edu.uiz.ac.ma

✉ J. A. Navio
   navio@us.es

1   Laboratory of Materials, Process, Catalysis and Environment, Higher School of Technology, University Sidi Mohamed Ben Abdellah, Fez, Morocco

2   Laboratory of Materials and Environment, Faculty of Sciences, Ibn Zohr University, Agadir, Morocco

3   Laboratory of Electromagnetic Processing of Materials (Ministry of Education), Northeastern University, Shenyang 110819, China

4   Instituto de Ciencia de Materiales de Sevilla, Centro Mixto, Universidad de Sevilla-CSIC, Américo Vespucio 49, 41092 Sevilla, Spain

5   Laboratoire de Biotechnlogie, Bioressources et Bioinformatique (3Bio), École Supérieure de Technologie de Khénifra, Université Sultan Moulay Slimane, Béni Mellal, Morocco

Introduction

Nowadays, water pollution due to the release of dyes from the textile industry has increased dramatically and is considered a major environmental issue threatening human health and sustainability [1–5]. Basic Blue 41 (BB41) is widely used in the textile industry, highly toxic, poorly biodegradable, and harmful to the environment [6–8].

Semiconductor materials with photocatalytic properties have been widely studied and used due to their potential applications for water splitting and pollution remediation from wastewater using solar energy [9–15]. Thus, conventional (and current) photocatalysts such as pristine ZnO and TiO_2 have been studied for the photodegradation of different molecules [9, 13, 16, 17]. However, these conventional photocatalysts are characterized by large bandgaps excited only by ultraviolet, which limits their use under UV illumination where they could only absorb 4% of the UV [18]. Consequently, visible light active photocatalysts (including

modified TiO_2 and ZnO) were designed and investigated as an efficient alternative to counteract environmental degradation under sunlight conditions [19–22].

Thus, improving the efficiency of other photocatalysts is needed for wastewater treatment. In this sense, ZnO became more interesting for wastewater treatment by photocatalytic process [19, 23–25]. Indeed, many studies report that ZnO is known for its high activity in solar light compared to TiO_2 [26]. The photodegradation of the majority of dyes is selective, incomplete, and in other cases are difficult to degrade because of their aromatic structures [27]. Moreover, some degradation processes produce secondary products which are in some cases even more harmful than the initial molecule [28]. An alternative method to replace the classical methods for dyes photodegradation is highlighted by semiconductor photocatalysts which have already been successfully applied for the degradation of various organic compounds [29–32]. In order to make ZnO appropriate for photocatalysis using solar light, various techniques such as metal or nonmetal doped ZnO nanoparticles were studied [22, 23, 33, 34]. It has been recognized that metal ions doping not only facilitates interfacial charge transfer reaction and enhances the photocatalytic activities of the semiconductor materials, but also modifies their absorption capacities [35]. Because of its abundant electronic states, cobalt was effectively used as a dopant metal in order to improve the electronic and optical properties of the ZnO lattice structure and generate a significant redshift in bandgap energy which favors the electron transfer and tuning of the Fermi level of ZnO [36, 37]. Nevertheless, few studies have been carried out to assess the photocatalytic properties of cobalt doped ZnO and their results showed that those catalysts could have a decent photocatalytic efficiency under visible light irradiation for the dyes' degradation [38]. Furthermore, up to now, there is no related theoretical study to probe the detailed mechanism underlying the cobalt doping effect in the ZnO matrix. Obviously, the improvement in the photocatalytic activity of cobalt-doped ZnO remains unclear.

On the other hand, one of the response surface methodology (RSM) designs, the Box–Behnken design (BBD) was applied in numerous types of research to optimize many operational parameters for wastewater treatment using different processes [39]. BBD is known for its economy in terms of few experimental tests compared to other RSM designs and efficiency for analyzing the process behavior and the statistical significance [40, 41].

The main objective of this work is to synthesize $Co_xZn_{1-x}O$ photocatalyst using the solution combustion method (SCM) with urea as a fuel source might lead to minimizing the bandgap energy and leading to new photoconversion properties. Therefore, in this work, we systematically highlight the influence of cobalt-doping on the optical properties and the photocatalytic activity of the ZnO under visible light. The

experimental results of cobalt-doped ZnO reactivity during BB41 dye degradation were investigated in the first place using the DFT calculations. Likewise, to the best of our knowledge, the degradation of basic dyes with photocatalysis was not sufficiently explored using response surface methodology. Hence, we used Box–Behnken design for the assessment of pH, [BB41], and doping amount of cobalt effect on the band structures and conversion efficiency. At the end of this work, a global mechanism was suggested to describe the possible photodegradation routes of BB41 by cobalt-doped ZnO. This work may be of interest to scientists working on such materials and would open up new prospects to design large-scale reactors for the treatment of large volumes of real wastewater.

Materials and methods

Preparation of catalysts

Zinc nitrate hexahydrate 98% [$Zn (NO_3)_2 \cdot 6H_2O$], cobalt nitrate hexahydrate 99.99% [$Co (NO_3)_2 \cdot 6H_2O$], urea 98% (NH_2CONH_2) as propellant fuel, and basic blue 41 98% ($C_{22}H_{16}N_2Na_2O_{11}S_3$) were provided by Sigma-Aldrich.

Firstly, the synthesis of ZnO as reference material and cobalt-doped ZnO was performed using the solution combustion method (SCM) as described in our previous article [29]. Cobalt ZnO is synthesized according to the reaction described by Eq. (1):

$$(1-x)Zn\,(NO_3)_2 6H_2O + x\,Co(NO_3)_2 6H_2O$$
$$+ y\,CH_4N_2O \xrightarrow{\text{water}} Co_xZn_{1-x}O \qquad (1)$$
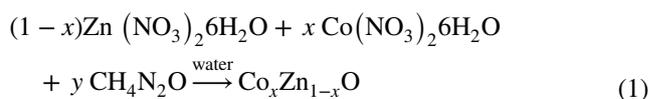
The prepared catalysts will be noted henceforth as $Co_xZn_{1-x}O$ ($x\%$), where $x = 0$; 10 and 20 where x is nominal molar percentages.

Characterization instruments

A diffractometer (X'PERT PRO) equipped with a detector of 40 kV and 30 mA with Cu Kα radiation ($\lambda = 1.54$ Å) was used to obtain X-ray diffraction (XRD) patterns.

Fourier-transform infrared analysis was carried out using the spectrometer (VERTEX 70) at ambient temperature in the range 400–4000 cm^{-1}.

X-ray fluorescence technique (XRF) was used to determine the chemical composition using Panalytical Axios sequential spectrophotometer equipped with Rh-tube as the source of radiation.

The Brunauer–Emmett–Teller surface area (S_{BET}) was estimated from nitrogen (N_2) adsorption/desorption data using Micromeritics ASAP2420.

Scanning electron microscopy (SEM) coupled to the energy dispersed spectroscopy (EDS) was used to investigate the catalysts' morphology.

The UV diffuse reflectance spectra (DRS) were obtained in the range 200–800 nm, using a UV–Vis spectrophotometer equipped with an integrating sphere (PerkinElmer Lambda 1050) and using $BaSO_4$ as reference.

Procedure of photodegradation experiments

Photocatalytic tests under visible irradiation conditions have been performed to assess the degradation of BB41 dye and to optimize its reaction conditions. The experiments were executed in a batch reactor (100 mL). Osram Ultra-Vitalux lamp (300 W) equipped with a polyester UV filter sheet (Edmund Optics) showing 99.9% of absorbance below 390 nm was used as an illumination source. In order to carry out a batch test, a selected amount of $Co_xZn_{1-x}O$ photocatalysts was added into 100 mL of BB41 dye solution volumes with different selected initial concentrations. The mixtures of photocatalyst and BB41 solutions were stirred in dark for 30 min in order to reach the adsorption–desorption equilibrium, then illuminated with visible light. Finally, the measurement of BB41 concentration was obtained by spectrophotometry method ($\lambda = 605$ nm) using a UV–visible spectrophotometer (J.P. SELECTA, S.A. VR-2000).

The conversion percentage of BB41 was obtained according to the formula (2); Where C_0 is the initial concentration (ppm) of BB41 and C_t is the concentration at the time of solution sampling:

$$\text{Conversion \%} = \frac{C_0 - C_t}{C_0} \times 100 \qquad (2)$$

At the end of each test, the total organic carbon (TOC) was measured using an analyzer (TOC-VCSN, Shimadzu) to verify the total mineralization of the BB41 in the solutions. TOC removal was obtained using the formula (3). Moreover, the measurement of TOC and BB41 concentration was taken in triplicate.

Chemical oxygen demand (COD) (mg $O_2 \cdot L^{-1}$) was measured using the closed reflux tube method (5220D).

$$\text{TOC (\%)} = \left[\frac{\text{TOC}_i - \text{TOC}_f}{\text{TOC}_i}\right] \times 100 \qquad (3)$$

Experimental design

Box–Behnken Design (BBD) was applied to examine and optimize the influence of the main parameters on BB41 degradation using $Co_xZn_{1-x}O$ as photocatalyst based on the response surface methodology.

Indeed, BBD was used to study the effect of pH, [BB41], and Co doping on the efficiency of photocatalytic degradation. The total number of experimental tests was obtained according to the formula Eq. (4):

$$N = 2^K + 2K + f \qquad (4)$$

where N, K, and f are the number of test runs, the factor number, and the number of replicates at the central point, respectively.

The correlation between a response (Y) and the variables (X_i, $i = 1, 2, 3$) is generally described by second-order polynomial Eq. (5):

$$Y = \beta_0 + \sum_{i=1}^{k} \beta_i X_i + \sum_{i=1}^{k} \beta_{ii} X_i^2 + \sum_{i \leq 1}^{k} \beta_{ij} X_i X_j + \varepsilon \qquad (5)$$

where Y is the studied response, β_0 is the intercept parameter; β_i, β_{ii}, and β_{ij} indicate the linear effects, the quadratic effects, and the interaction effects, respectively. X_i and X_j are the optimized factors and k is their number, and ε is the random error.

In order to investigate the fitting of the observed results with the prediction model and its accuracy, the analysis of variance (ANOVA) was used on the basis of the determination coefficient (R^2 and adjusted R^2) and p-value (probability) ($p < 0.05$).

Computational methodology

In this study, we consider $2 \times 2 \times 2$ supercells (containing 32 atoms, 16 of Zn, and 16 of O) with the space group symmetry of P63mc. In each supercell, we have substituted two atoms of Zn by two atoms of Co in order to reach 12.5% and three atoms of Zn by three atoms of Co to obtain 18.75% of doping concentration. All calculations were carried out by using DFT with a plane-wave basis set and pseudopotentials, as implemented in the quantum-ESPRESSO package [42]. Exchange and correlation effects are approximated using the generalized-gradient-approximation (GGA) as parametrized by Perdew, Burke, and Ernzerhof (PBE) [43]. The GGA + U method with a Hubbard-like on-site correction was employed to correct the value of bandgap of ZnO, and the U values employed in this work are U (d; Zn) = 10 eV, U (p; O) = 7 eV, and $U(d$; Co) = 6 eV. The electron–ion interaction is represented using ultrasoft pseudopotentials (USP). The cutoff for the kinetic energy was set at 50 Ry for the Kohn–Sham orbitals and to 550 Ry for the charge density. A $4 \times 4 \times 4$ Monkhorst–Pack grid was used for the k-point sampling of the Brillouin zone [44]. The convergence threshold for the self-consistent-field iterations was set to 10^{-6} Ry. The

standard Broyden–Fletcher–Goldfarb–Shanno (BFGS) method was used for the structural optimizations until the force on each atom was less than 10^{-3} Ry/(a.u).

Results and discussion

Table 1 presents the textural properties and chemical composition of the synthesized cobalt doped ZnO samples. It is observed that the catalysts have a relatively low surface area, which could be explained by the presence of the intrinsic combustion process applied. However, the specific surface area increases slightly with the incorporation of increasing amounts of cobalt. It is also observed that a raising in the percentage of cobalt leads to a reduction in the crystallite size, which correlates with the slight augmentation in the specific surface area observed. This fact indicates that the incorporation of cobalt modifies not only the textural properties of the samples but also the crystallite size. Moreover,

Table 1 Textural properties and chemical composition of cobalt doped ZnO samples

Catalyst	S_{BET} (m²/g)	Crystallite size (nm)	% XRF		
			Zn	Co	O
ZnO	3.4	18.56	–	–	–
10% cobalt doped ZnO	5.2	16.71	74.15	7.31	17.63
20% cobalt doped ZnO	7.7	12.11	67.50	15.07	16.52

XRF analysis was used to confirm the nominal molar percentage of the final products which shows that the synthesized catalyst was cobalt doped ZnO with a Co: Zn molar ratio of 0.1/0.9 and 0.2/0.8.

Characterization

The XRD patterns of $Co_xZn_{1-x}O$ ($0 < x < 0.2$) nanoparticles are displayed in Fig. 1. The diffractogram indicates a high matching between the corresponding peaks and the standard pattern of pure ZnO (JCPDSNo.36-1451). XRD patterns of pure and cobalt doped ZnO catalysts show the hexagonal wurtzite phase was well-formed (Fig. 1A). Furthermore, no secondary phase of cobalt or any other compound was noticed for cobalt-doped ZnO nanoparticles, thus indicating that the hexagonal ZnO phase was intact [45].

Figure 1B presents the enlarged XRD patterns in the range 45–50° of pure ZnO and $Co_xZn_{1-x}O$ materials. The figure shows a noticeable shifting and broadening in peaks position toward a higher 2θ value corresponding to that of pristine ZnO with rising cobalt percentage. The shifting of the 2θ position of XRD patterns demonstrates a slight variation of the lattice parameters of ZnO with cobalt doping because the radius of Co^{2+} (0.65 Å) is less than the Zn^{2+} radius (0.74 Å). Moreover, Fig. 1B shows that the diffraction peak intensities were diminished with a rising of cobalt amount in the ZnO phase, confirming then the successful substitution of dopant Co^{2+} ions in the ZnO structure [46, 47]. The calculation of the average crystallite size of the synthesized catalyst was obtained following Debye–Scherrer's Eq. (7) [48].
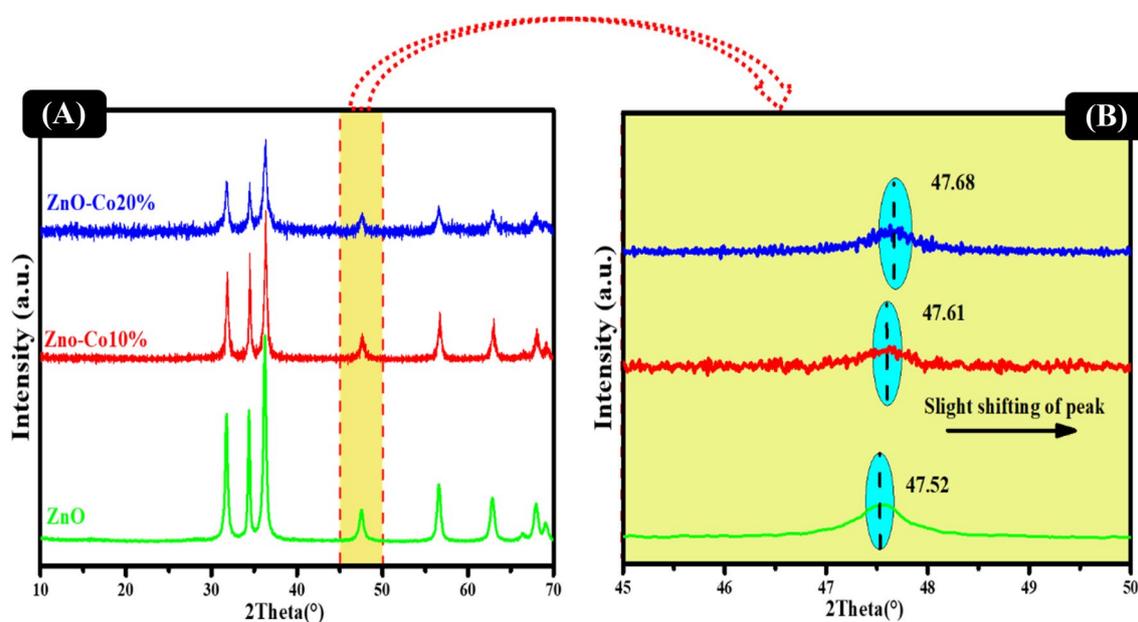

Fig. 1 **A** XRD patterns of undoped and Co-doped ZnO catalysts; **B** The enlarged XRD patterns from 45° to 50° of (**A**)

$$D = \frac{K\lambda}{\beta c.\text{Cos}\theta} \qquad (6)$$

where k is the shape factor ($k=0.94$) and λ is the wavelength of X-ray; Θ is the Bragg angle and βc is the corrected line broadening defined as full width at half maximum (FWHM). The growth of the full width at half the maximum of the diffraction peak indicates a diminution of the crystallite size with rising cobalt amount in the ZnO structure. The average crystallite size of pristine ZnO catalyst is calculated to be 18.56 nm, with a rise in cobalt percentage, the latest value decreases as illustrated in Table 1. The diminution in the average crystallite size could be explained by the distortion in the ZnO structure by the incorporation of cobalt impurity which reduces slightly the nucleation and growth rate of ZnO nanoparticles, and the formation of slight stress is possibly due to the variation in the ion size between Zn^{2+} (0.740 A˚) and Co^{2+} (0.65 A˚) [49, 50].

It is worth noting that according to the literature report, the substitution limit of Co^{2+} ions in ZnO to be 30% [51, 52]. Many reports are available in the literature on the low doping concentration of Co^{2+} ions in the ZnO matrix. To the best of our knowledge, no detailed study reports on the effect of higher Co^{2+} doping concentration on the structural, optical, and photocatalytic properties of ZnO nanoparticles.

On the other hand, by using the XRD technique we observed a small amount of impurity peak or secondary phase (Co_3O_4) after $x \geq 0.20$ mol, which may be due to the doping limit of Co^{2+} ions in the ZnO matrix. These results are in good consent with the literature [53, 54]. Beyond the solubility limit of cobalt, the formation of CoO and/or Co_3O_4 structures in contact with the ZnO surface could generate a heterojunction that would affect the photocatalytic properties of the system. This study requires more attention and possibly because of this, the system with a high content of cobalt ions has not been studied.

SEM analysis was carried out to study the morphology of the 20% cobalt doped ZnO catalyst (the optimal photocatalyst). Figure 2A, B shows the selected images of the 20% cobalt-doped ZnO catalyst at different magnifications. As shown the 20% cobalt-doped ZnO sample is composed of high amounts of quasi-laminated shape particles with a size of 2–10 μm. EDS mapping analysis was occurred to determine the elements contained in the synthesized 20% cobalt doped ZnO catalyst and to examine its elemental distribution. Figure 2C shows the mapping distribution of Co, Zn, and O confirming then the absence of any element as an impurity which proves the high purity of as-synthesized 20% cobalt doped ZnO catalyst. A detailed observation of the images in Fig. 2A shows some particles with different morphologies (almost rounded) in contact with the larger particles, which in a previous article were identified as CoO_x [49]. In fact, in the images of Fig. 2C, it can be observed that

there are zones where the sample shows a cobalt enrichment. According to this observation, the successful synthesis of cobalt doped ZnO could be well accepted, despite the partial segregation of cobalt that has occurred on the catalyst surface in the form of CoO_x, probably as Co_3O_4, next to the doping cobalt.

The UV–Vis spectra of the cobalt-doped ZnO catalyst were used to investigate its optical properties. Figure 3 displays the absorption spectra of the undoped and cobalt-doped ZnO catalysts. By comparing to pristine ZnO (Fig. 3A) which absorbs only in the UV range ($\lambda < 400$ nm) matching to the bandgap transition of ZnO structure, the cobalt-doped ZnO exhibits an important absorption in the visible range ($\lambda > 400$ nm) suggesting a reduction in the bandgap energy value. This decline could be explained by the oxygen defects, resulting in an excess of free electrons over the valence band and potentially new introduced energy levels, which is possibly caused by $sp\text{-}d$ exchange interactions between band electrons and localized d electrons of Co^{2+} ions. Consequently, this finding enhances the photocatalysis activity under visible light [55–57].

As Co-doped ZnO is a magnetic material, it exhibits two bandgaps, spin-up bandgap, and spin-down bandgap. Therefore, the bandgap is the energy between the highest density of states before the Fermi level (valence band) and the first density of state after the Fermi level (conduction band). Hence, the optical bandgap (E_g) values were estimated from Tauc plots calculated using the Kubelka–Munk function [58] of pure ZnO and cobalt doped ZnO catalysts using the following formula [59]:

$$(\alpha h v)^2 = A\left(h v - E_g\right) \qquad (7)$$

where h, v, α, and A are Plank's constant, photon frequency, absorption coefficient, and a constant, respectively. The optical bandgaps can be determined by extrapolating the linear region of $(\alpha h v)^2$ versus the photon energy axis (Fig. 3B). The calculated bandgaps are 3.18, 2.82, and 2.67 eV for ZnO, 10% cobalt doped ZnO, and 20% cobalt doped ZnO crystals, respectively. After the insertion of cobalt ions, the bandgap of ZnO was intrinsically changed. This finding is similar to that of a previous work, which showed that adding Co to ZnO could narrow its optical bandgap [60, 61].

The electronic structure of as-prepared catalysts was calculated by density functional theory (DFT) since it substantially impacts the photocatalyst activity in the band of conduction and valence. Based on the density of states (DOS) of the pure ZnO (Fig. 4A), it can be seen that the valence band consists of three groups. The O2p states are responsible for the upper valence band from -7.0 to 0 eV, while the Zn 3d states lead to the lower valence band from -8.0 to -5.1 eV. The O2s states are the origin of the lowest valence band from -16.0 to -14.1 eV, with a minor

Fig. 2 **A** and **B** SEM images of 20% cobalt doped ZnO catalyst at two different magnifications; **C** EDS elemental mapping images of 20% cobalt doped ZnO catalyst
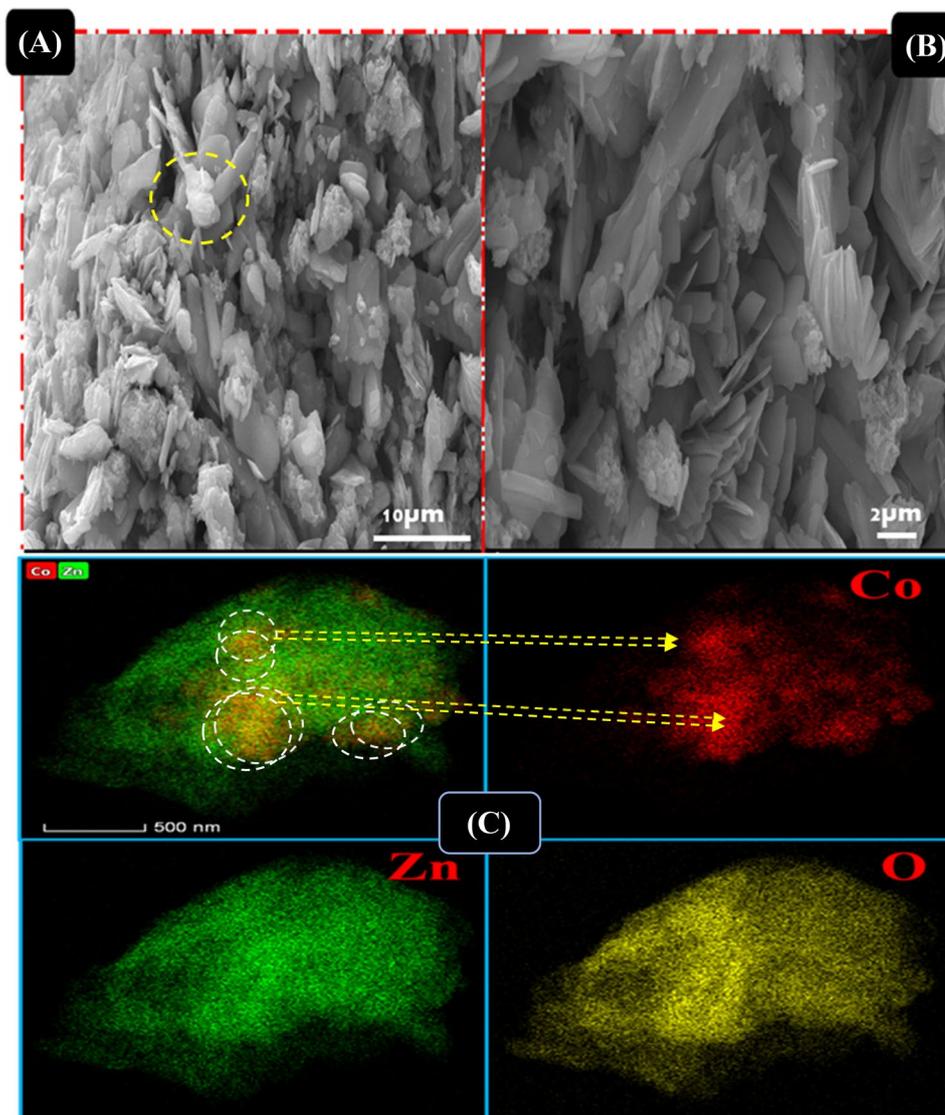
contribution from the Zn 4*s* orbital level. The CB, on the other hand, is primarily made up of the O2*p* and Zn-4*s* hybrid states.

Once Co is incorporated into ZnO (Fig. 4B, C), the apparition of new electron states is noticed at the valence band and conduction band [56, 62]. The VB is dominated by Zn 3*d* and O2*p* orbitals, with some Co 3*d* orbitals, while the CB is dominated by Co 3*d*, O2*p*, and Zn 4*s* orbitals in addition to a minor contribution from O(2*s*) orbitals. The electronic transition of O 2p → Co 3*d*, O2*p* → Zn 4*s*, Zn 3*d* → O2*p*, and Co 3*d* → O2*p* states are responsible for the visible light absorption of cobalt doped ZnO. Principally, in cobalt doped ZnO, the electronic transitions of Zn 3*d* → O2*p* and O2*p* → Co 3*d* states are considerably stronger than in other doped systems, resulting in significantly increased visible light absorption. This could explain the high photocatalytic activity exhibited by the cobalt-doped ZnO.

The calculated bandgap of pure ZnO, 12.5% cobalt doped ZnO, and 18.75% cobalt doped ZnO is lower than the experimental values and is about 3.27 eV, 2.75 eV, and 2.61 eV, respectively. This is mainly owing to the use of generalized gradient approximation (GGA) exchange–correlation energy in DFT simulation. The GGA, on the other hand, may provide a more reasonable change of different bandgap values after doping, and the evolution is consistent with the UV–vis data displayed in Fig. 3B.

pH_{pzc} is also considered as a critical parameter to characterize the catalyst surface charge in different pH medium values. Indeed, the pH_{pzc} value of cobalt doped ZnO is obtained following the drift method [63]. Hence, Fig. 5 illustrates the variation of pHfinal as a function of $pH_{initial}$ and the pH_{pzc} value corresponds to the intersection of this curve with the line $pH_{initial} = pH_{final}$ which equals 9.4 for the cobalt doped ZnO surface.
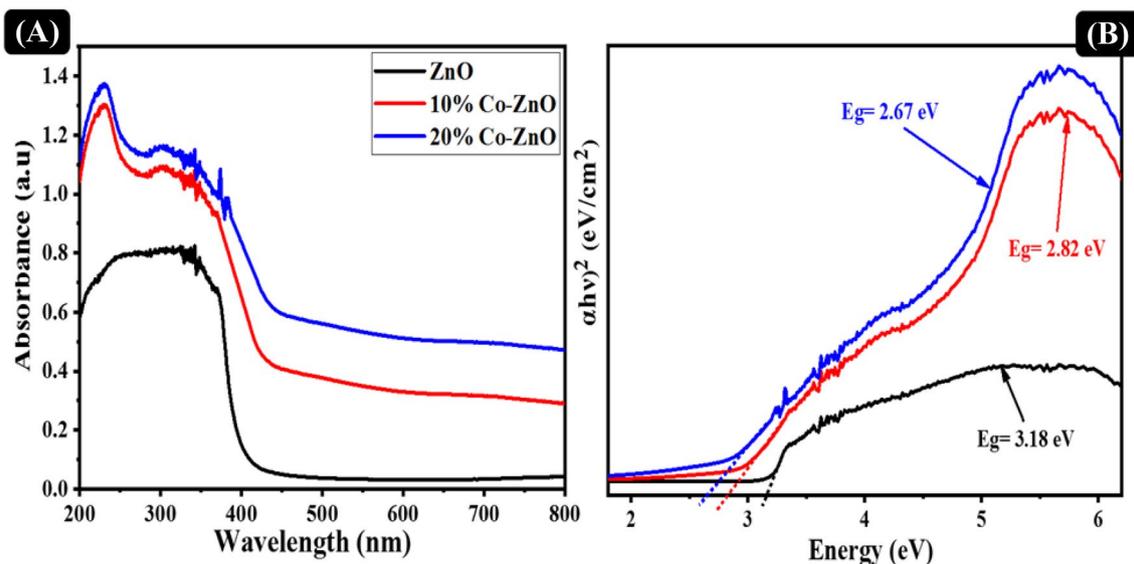
Fig. 3 **A** DRS spectra of undoped and cobalt doped ZnO catalysts. **B** $(\alpha h\nu)^2$ versus hv plot for undoped and cobalt doped ZnO catalysts
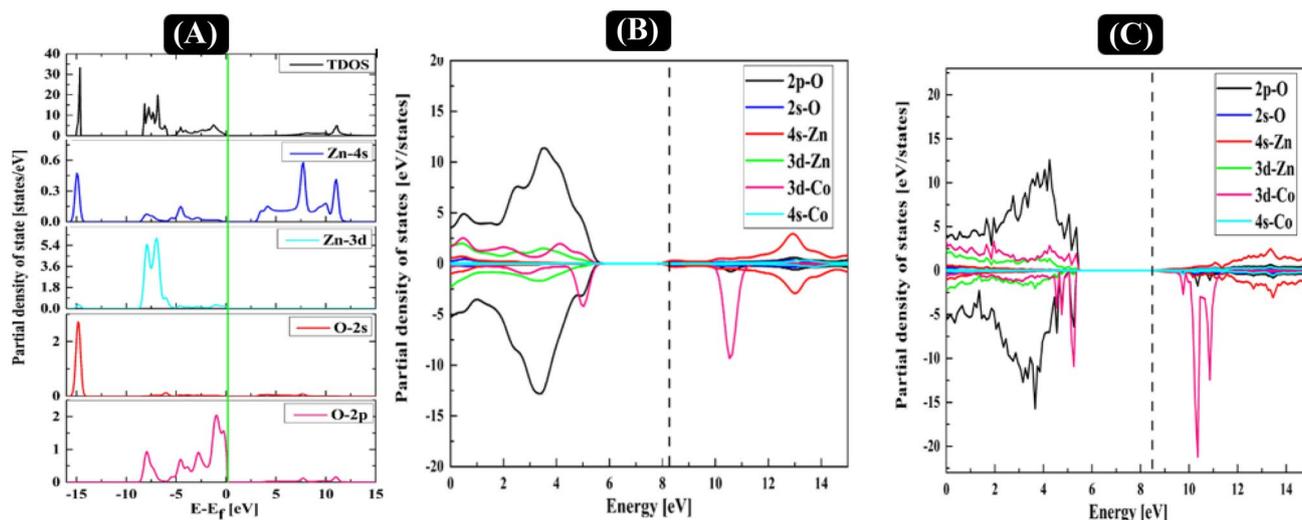

Fig. 4 Density of states (DOS) of **A** ZnO, **B** 12.5%cobalt doped ZnO and **C** 18.75% cobalt doped ZnO

Optimization of photodegradation of BB41

The effect of the key parameters was explored using the Box–Behnken design: pH (X_1), [BB41] (X_2), and Amount of Co as doping agent (X_3) on the BB41 conversion response (Y_1), with the objective of maximizing the response value. According to preliminary tests, each factor was varied in a range: X_1 (4–12), X_2 (10–30 ppm), and X_3 (0–20%). Where the corresponding data are given in Table 2. As a result, the experimental results were processed and designed using the NemrodW software. The findings were evaluated using the analysis of variance test (ANOVA), with the determination coefficient (R^2 and adjusted R^2) and p-value (probability) with a 95% confidence level ($p < 0.05$) as the key parameters used to assess the model's efficacy significance and prediction efficiency [64].

Table 2 represents the three variables studied and their corresponding levels. The contact time is set at 120 min (supposedly optimum value).

The total number of experimental tests used in this work is 17, which was determined using the formula $N = 2 \times k \times (k - 1) + C_0$, where $k = 3$ is the number of the factors studied and $C_0 = 5$ is the number of central points. Thus, the matrix of 17 experiments obtained by BBD and
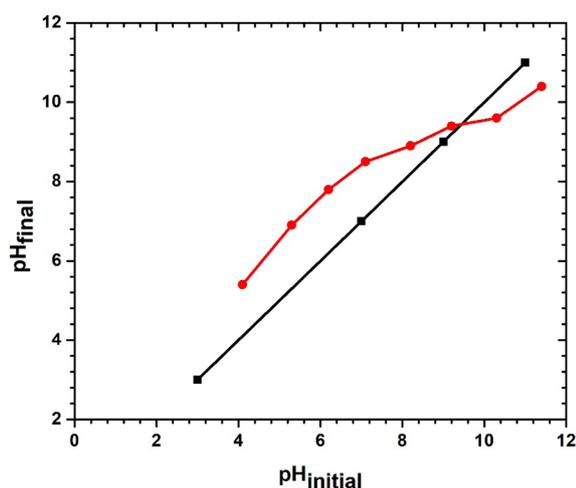
Fig. 5 pH of zero-point charge of cobalt doped ZnO powder

Table 2 Coded and actual values of operational parameters for the Box–Behnken plan

Factors	Coded and real value		
	− 1	0	+ 1
pH X_1	4	8	12
BB41 concentration (ppm) X_2	10	20	30
Molar amount of Co as doping (%) X_3	0	10	20

Table 3 Box–Behnken design for the three independent variables with observed and predicted responses to BB41 dye conversion (%)

Experiment	pH	[BB41] (ppm)	Co amount (%)	Conversion (%)
1	4	10	10	37.00
2	12	10	10	74.00
3	4	30	10	30.00
4	12	30	10	67.00
5	4	20	0	20.00
6	12	20	0	24.00
7	4	20	20	42.00
8	12	20	20	99.00
9	8	10	0	28.00
10	8	30	0	23.00
11	8	10	20	88.00
12	8	30	20	81.00
13	8	20	10	55.00
14	8	20	10	54.00
15	8	20	10	54.00
16	8	20	10	55.00
17	8	20	10	56.00

postulated model is confirmed by a value of Fisher high (F) with a probability (p) as low as possible. From the ANOVA test of the reaction, the p values (< 0.01) evaluated much lower than 0.05 confirm that the model term is significant. The model was considered highly significant based on the high Fisher test ($F = 1436.65$) with a very low probability value ($p < 0.01$). In addition, the comparison of the critical F value ($F0.05, 9, 9 = 3.179$) with the calculated F value ($F = 1436.65$) showed an F critical value lower than the calculated F value, and it appears thus that the model is well adapted to the experimental data [65, 66].

From the ANOVA Table 4 above, we conclude that the chosen statistical model is validated because we have:

$- p - \text{value} = 1\% < 5\%$
$- R^2 = 0.991 > 0.8$
$- R^2aj = 0.98 > 0.7$

The Student's test is a statistical test that makes it possible to judge the significance of the effect coefficients. Generally, coefficients that have a significance less than 5% consider themselves as coefficients having a significant effect on

their corresponding responses are listed in Table 3. Experiments 13, 14, 15, 16, and 17 represent the experiments at the center.

Table 4 shows the results of the ANOVA used to verify the model validity of this study. Indeed, the model's p-value for BB41 conversion is less than 0.01, suggesting the high statistical significance of the model. Furthermore, the regression coefficient values (R^2 and adjusted R^2) for conversion response are closer to 1 (between 0.99 and 0.98). Therefore, this result shows that the model is in good fit with the experimental data for BB41 conversion response.

The quadratic model presented by Eq. (8) is obtained by the regression between the dependent variable (BB41 conversion) and the coded values of the three independent variables:

$$Y = 54.80 + 16.87 * X_1 - 3.25 * X_2 + 26.87 * X_3 - 5.77 * (X_1 * X_1)$$
$$+ 2.97 * (X_2 * X_2) - 2.77 * (X_3 * X_3) + 13.25 * (X_1 * X_3) - 0.5 * (X_2 * X_3)$$

(8)

Analysis of the variance (ANOVA) was used and the results are given in general, the adaptation of the

the response. The following Table 5 groups the calculated statistics:

Table 4 ANOVA variance analysis results

Source	Sum of squares	Degree of freedom	Mean square	Ratio	Signification (%)
Regression	9.05092E+0003	9	1.00565E+0003	1436.6541	< 0.01***
Residuals	7.95500E+0001	7	1.13642E+0001		
Lack of fit	7.67500E+0001	3	2.55833E+0001	36.5476	0.230**
Pure error	2.80000E+0000	4	7.00000E−0001		
Total	9.13047E+0003	16			

$R^2 = 0.991$, Adjusted $R^2 = 0.980$, Predicted $R^2 = 0.865$

Table 5 Estimated regression coefficient and the F and p values obtained during the design of Box–Behnken

Coefficient	Estimate coefficient	Inflation factor	Standard deviation	t.ratio	Signification
$b0$	54.800		0.37416574	146.46	< 0.01 ***
$b1$	16.875	1.00	0.29580399	57.05	< 0.01 ***
$b2$	− 3.250	1.00	0.29580399	− 10.99	0.0390 ***
$b3$	26.875	1.00	0.29580399	90.85	< 0.01 ***
$b1$-1	− 5.775	1.01	0.40773766	− 14.16	0.0144 ***
$b2$-2	2.975	1.01	0.40773766	7.30	0.188 **
$b3$-3	− 2.775	1.01	0.40773766	− 6.81	0.244 **
$b1$-2	0.000	1.00	0.41833001	0.00	100.0
$b1$-3	13.250	1.00	0.41833001	31.67	< 0.01 ***
$b2$-3	− 0.500	1.00	0.41833001	− 1.20	29.8

t.ratio. is the value of variables determined by Student's test

**$p < 1\%$

*$p < 5\%$

***Significant for $0.0001 < p$ value < 0.001

**Significant for $0.001 < p$ value < 0.01

*Nonsignificant for p value > 0.05

These results (Table 5) show that doping cobalt with different amounts is the most significant factor on the BB41 degradation, followed by pH and its quadratic effect. Thus, cobalt amount doping affects the conversion positively, which means that BB41 conversion enhances with increasing cobalt amount in the ZnO matrix, this could be explained by the energy value decline of the bandgap, and it accords with its high and positive t-ratio (90.85). However, [BB41] has a significant negative impact on response with a t-ratio of − 10.9, demonstrating that degradation effectiveness decreases with rising [BB41] initial concentration, which is in accordance with previous researches approving that the photodegradation process is disfavored at high dye concentration [6]. The residuals versus the predicted responses and normal plot probability of the responses residuals are displayed in Fig. 6A and show a slightly random arrangement of the residuals proving the adequacy of the models [67].

Figure 6B shows that all the values of the residuals line up well on Henry's line and follow a normal distribution. Thus, the mathematical model is validated, and each second-order model has been found to be applied as a prediction equation [67].

The desirability plot corresponding to the BB41 conversion response was illustrated in Fig. 7. It shows the desirability reaches its maximum for BB41 conversion of 85% when cobalt amount doping was equal to 20%, pH value attained 11, and [BB41] of 26 ppm.

Canonical analysis Fig. 8 graph confirms what has been found in the graph of desirability. In effect more we move toward the higher factors levels the BB41 conversion increases. As a result, the three parameters X_1, X_2, and X_3 must be at their high levels for a good BB41 conversion [68].

The three-dimensional (3D) response surface plots and the corresponding contour curves investigate the effect of the interaction terms. Figure 9 shows the response surface for the mutual effects of cobalt amount doping pH and [BB41]. As shown in Fig. 9B, D and F increasing the cobalt amount doping and pH along with a decrease in [BB41] leads to increased BB41 conversion (%) at the fixed contact time of 120 min.

Each 3D response surface plot for BB41 conversion presents the effect of two independent variables on a response. Most plots show clear peaks indicating the optimum area of factors values for a maximum response value. Figure 9A, C

Fig. 6 **A** Graphic study of the residues of the response (BB41 degradation) and **B** Probability versus residuals for BB41 degradation
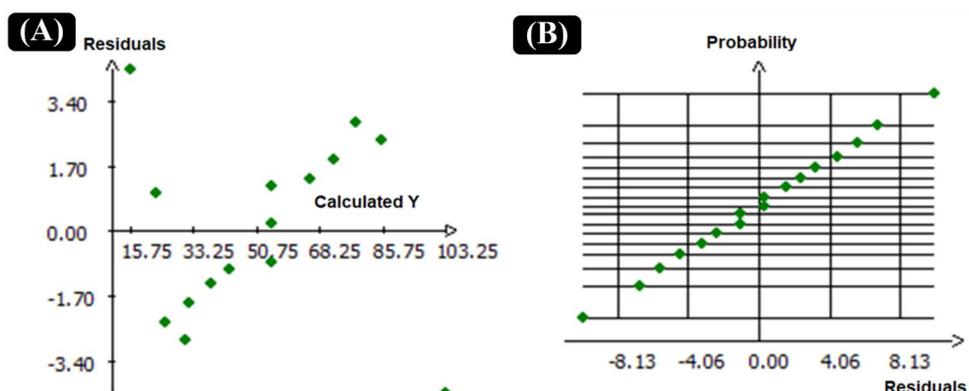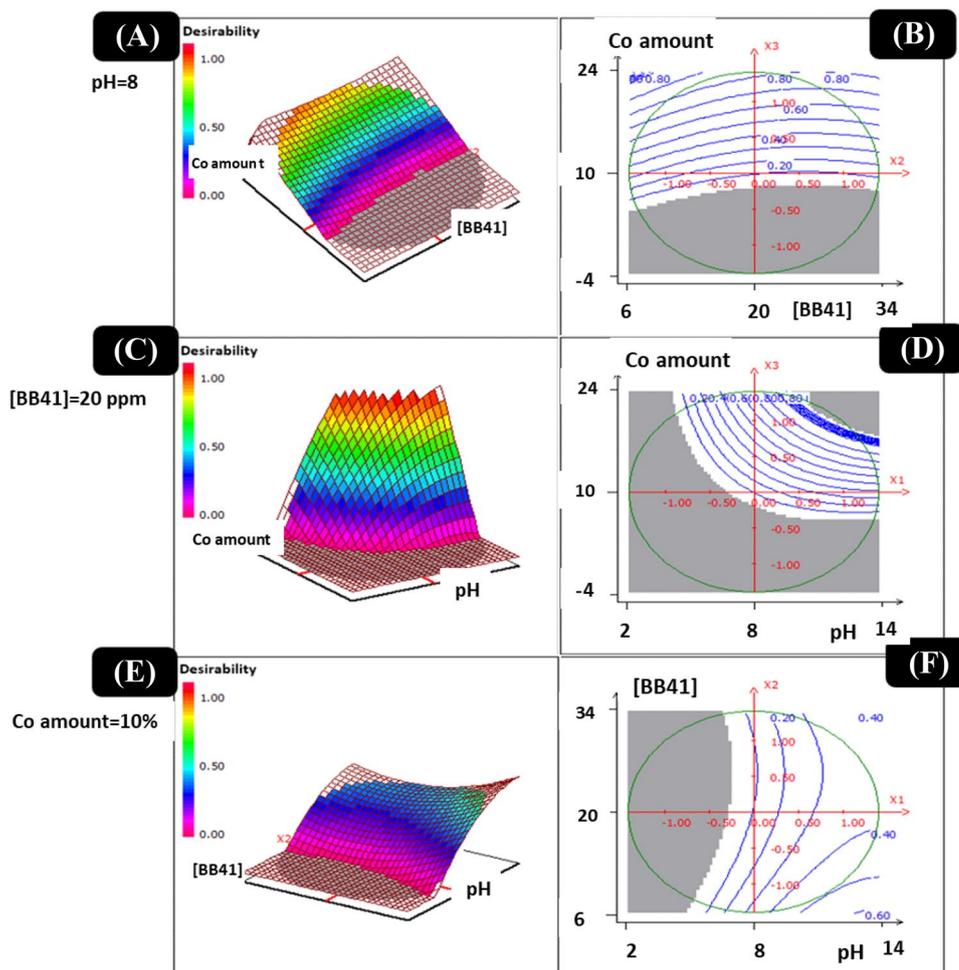

Fig. 7 2D and 3D plots of the desirability function with varying process parameters

and E demonstrates that increasing cobalt amount doping from 0 to 20% enhanced BB41 conversion from 30 to 80%. The result corresponds to previous studies approving that a high amount of cobalt in the ZnO matrix decreases the bandgap energy. While, varying pH dosage from 4 to 12 had a significant effect on BB41 conversion, and that could be due to the high pH value favoring the OH˙ generation which enhances BB41 degradation [69, 70].

Optimization of factors for BB41 conversion

The potential of the $Co_xZn_{1-x}O$ nanoparticles for the degradation of the BB41 molecules solution was carried out using the optimal conditions found by the experimental design (Table 6). The 20% cobalt doped ZnO catalyst displays a high conversion of 95% during 120 min of visible light illumination.
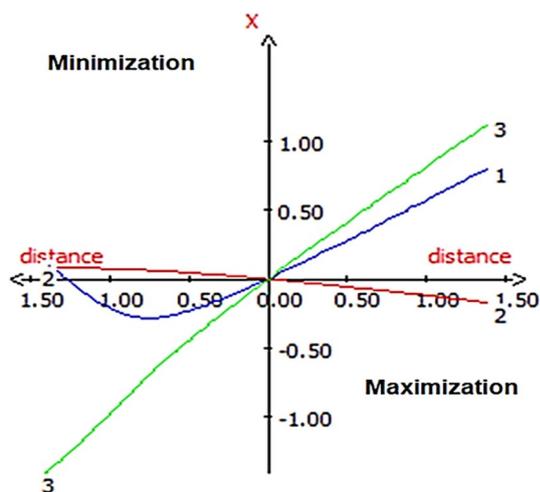
Fig. 8 Canonical analysis graph of the optimal path for the BB41 degradation

Figure 10A illustrates the BB41 degradation using the optimum conditions obtained from Box–Behnken response surface methodology. From Fig. 10A it is clearly seen that BB41 degraded (100%) within 120 min using 20% cobalt

doped ZnO catalyst which is in accordance with the predicted BB41 conversion provided by the Box–Behnken model.

Cycles of photocatalytic tests

In addition to the significant efficiency of the synthesized cobalt-doped ZnO for the degradation of organic dyes from aqueous solutions, stability is critical for choosing efficient photocatalysts. Figure 10B presents the degradation efficiency of BB41 (26 ppm) after two hours of visible light illumination, where the same high percentage of BB41 conversion is noticed (~ 90%) after each cycle. During the five reuse tests, the TOC values revealed a small decrease in mineralization efficiency. These results reveal that the photocatalyst maintains its stability after sequential cycles. The negligible decrease in photocatalytic efficiency was due in part to the unavoidable loss of photocatalyst mass during the washing and centrifugation processes [71].

Kinetic data in Fig. 10C present linear regressions of in (C_0/C) with the photodegradation time, which shows that the photodegradation of the BB41 follows the pseudo-first-order kinetics [67] described by the following equation:

Fig. 9 2D and 3D response surface plots for BB41 conversion depending to the variation of two factors (pH, [BB41]); (pH, Co amount); ([BB41], Co amount). Catalyst mass = 1 g/L; Irradiation time = 60 min
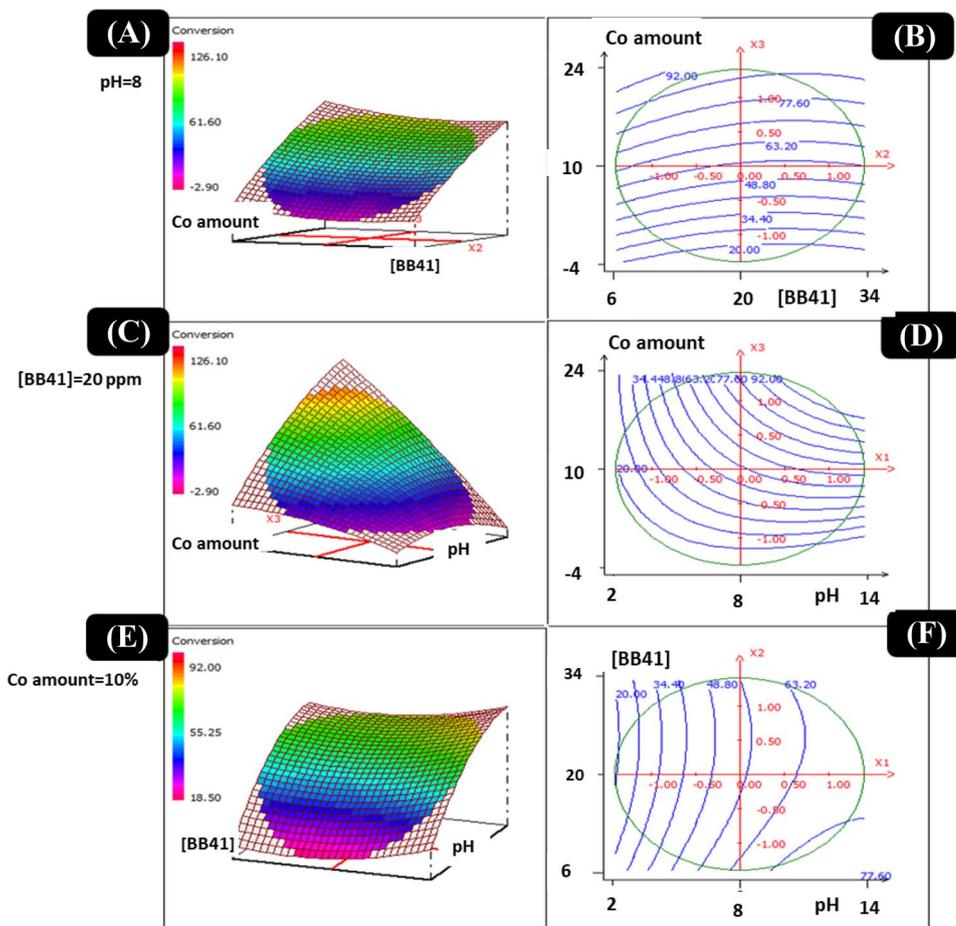
Table 6 Predicted and experimental values of BB41 conversion under optimal conditions

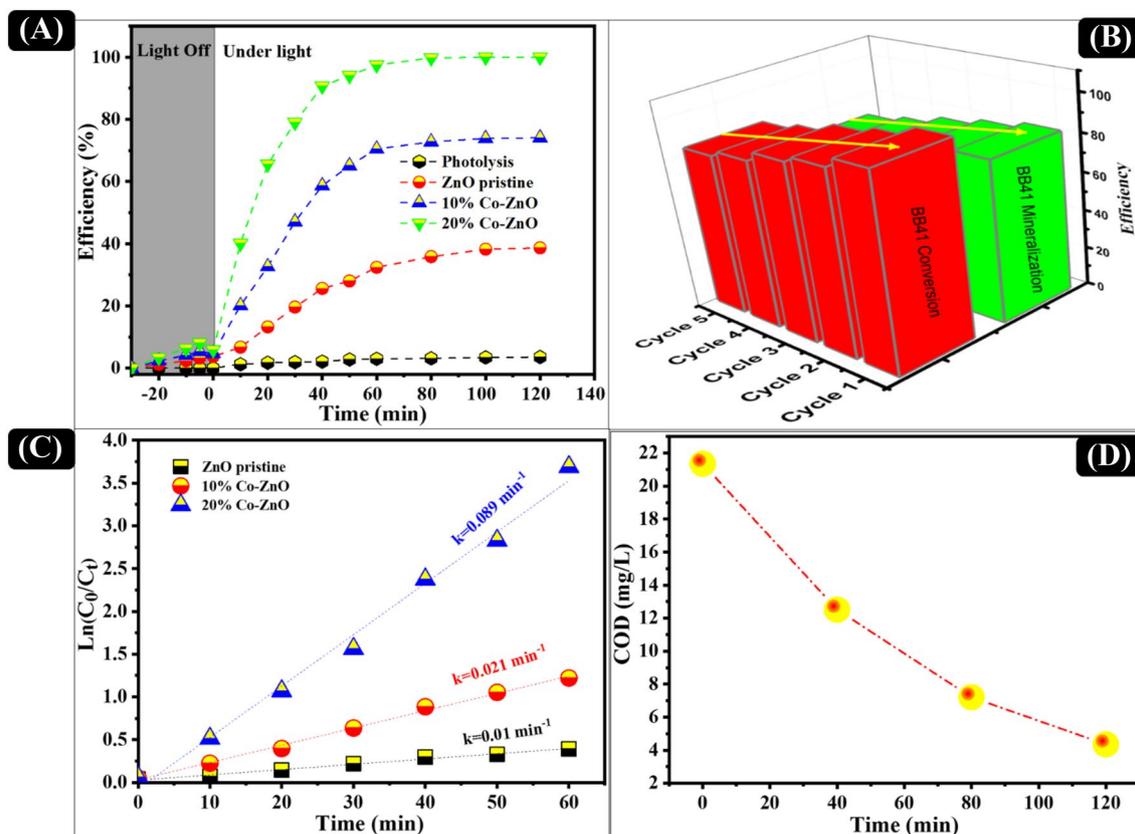| Variable	Factor	Value	BB41 conversion (%)	
X_1	pH	11	Optimum combination of the model 95	Experimental validation of the model 100
X_2	[BB41]	26		
X_3	Cobalt doping	20		

Fig. 10 A BB41 photodegradation under visible illumination, using 20% cobalt doped ZnO under optimum conditions; **B** Conversion (red) and mineralization (green) percentages during the consecutive's cycles for the BB41 conversion; **C** ln (C_0/C) versus time plot of BB41 conversion using cobalt doped ZnO catalyst; **D** COD of BB41 conversion over cobalt doped ZnO catalyst

in (C_0/C) = kt. Where C_0 and C_t are the initial and actual concentration of BB41 at time t, respectively, and k is the photodegradation rate constant [72, 73]. For $x = 0$, $x = 0.1$, and $x = 0.2$ in the Co$_x$Zn$_{1-x}$O system, the degradation rate constants were experimentally calculated to be 0.010 min^{-1}, 0.021 min^{-1}, and 0.089 min^{-1}, respectively. The enhancement of BB41 photodegradation under visible light irradiation is obviously noticed due to doping Co^{2+} ions in the ZnO matrix.

The results of the COD removal over 20% cobalt doped ZnO are illustrated in Fig. 10D, as shown, using this catalyst, a maximum removal percentage of COD (81.8%) was reached under the optimum conditions concluded from the

Box–Behnken design. This confirms the previous results mentioned above.

The characteristic peaks of BB41 before degradation were obtained by FTIR spectrum (Fig. 11A) in the fingerprint region (500–3500 cm^{-1}). The C–C stretching and bending vibrations of C–H in the benzene rings are indicated by peaks at 1640.21 cm^{-1} and in the 670.49–774.47 cm^{-1} region, respectively. Moreover, the peak at 1090.3 cm^{-1} corresponds to the presence of C–OH stretching vibrations. The existence of –OH groups on the surface of BB41 is indicated by the broad and intense vibration around the range 3000–3500 cm^{-1}. The FTIR spectra of BB41 after 60 min under visible light illumination shows that some peaks were
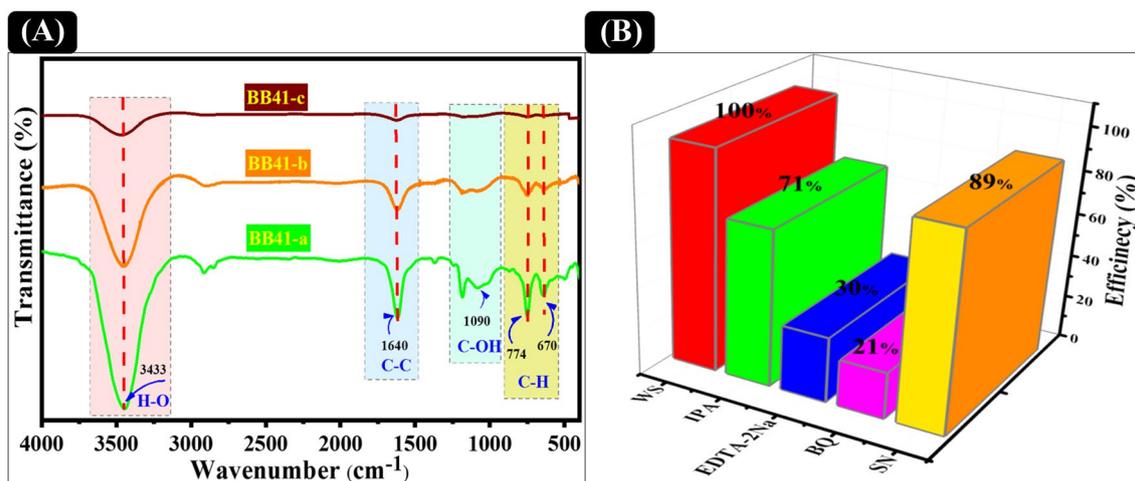
Fig. 11 **A** FT-IR spectra of BB41 during the photocatalytic process at times: **a** 0 min, **b** 40 min, **c** 90 min under the optimized conditions; **B** Trapping experiment of active species during BB41 conversion using 20% cobalt doped ZnO

disappeared, and the intensity becomes lower. In addition, more peaks were disappeared after 120 min which confirms the successful oxidation of BB41 molecules by hydroxyl radicals action [74].

Photodegradation mechanism

In order to investigate the photodegradation mechanism of BB41 conversion, radical scavenging tests were carried out to determine the responsible radicals and holes during the BB41 degradation. The holes (h^+), hydroxyl radical (OH·), electrons (e^-), and superoxide radical ($O_2^{·-}$) are snared by adding isopropanol (IPA) as OH· scavenger, Ethylene diamine tetra-acetic acid (EDTA-2Na) as h^+ scavenger, silver nitrate (SN) as e^- scavenger and benzoquinone (BQ) as $O_2^{·-}$ scavenger into the reaction medium, respectively, during the process of BB41 conversion [35, 75–77]. The scavenger test was based on adding 10 mg of 20% cobalt-doped ZnO catalyst, and 10 mM of radical scavengers to 50 mL of 26 ppm BB41 solution; then, the mixture was illuminated under the same conditions. Lastly, the BB41 conversion was measured and the active species were fixed. Figure 11B shows the conversion percentage using different scavengers. The photodegradation of BB41 slightly varied by the addition of IPA and SN. Nevertheless, the conversion is significantly decreased from 100 to 21 and 30% with the addition of a scavenger for ($O_2^{·-}$) and (h^+), respectively. Hence, it can be concluded that the superoxide radical and the holes are the responsible reactive species during BB41 photodegradation.

To study the optical properties of 20% cobalt doped ZnO catalyst, the valence band edge positions were determined using the following empirical equations (Eqs. 9–11) [78]:

$$\chi = \left(A^a + B^b + C^c\right)^{1/a+b+c} \tag{9}$$

$$E_{CB} = \chi - E_e - 0.5E_g \tag{10}$$

$$E_{VB} = E_{CB} + E_g \tag{11}$$

where χ (eV) is the absolute electronegative of as prepared 20% cobalt doped ZnO. *A*, *B*, and *C* are the absolute electronegativity of atm. E_{CB} (eV), E_{VB} (eV), and E_g (eV) are the VB edge potential, CB edge potential, and the bandgap energy of the semiconductors separately. E_e (eV) denotes the energy of free electrons on the hydrogen scale ($\approx$ 4.5 eV/NHE). Thus, the absolute electronegativity value of 20% cobalt doped ZnO photocatalyst was calculated to be 5.77 eV, the E_{CB} (eV), E_{VB} (eV) potentials are determinates to be − 0.59 eV and 2.61 eV one-to-one.

On the basis of the above results, the possible mechanism of enhanced photocatalytic performance over 20% cobalt-doped ZnO photocatalyst under visible illumination was proposed and shown in Fig. 12. Under Visible light illumination, the photogenerated electrons could transfer from: (1) from VB to CB of ZnO; (2) the valence band (VB) of ZnO to the localized Co energy levels and (3) from CB of ZnO to localized mid-gap states of Co and defects. This process inhibits e^-/h^+ recombination. Furthermore, it is possible that the adsorbed (O_2) could effectively capture the photogenerated electron for organic contaminant degradation by producing reactive $^•O_2^-$ radicals, and the photogenerated holes could be used as effective active sites. According to the radical scavenger experimental results, it was suggested that the photocatalytic process with the 20% cobalt doped ZnO catalyst was mainly due to the formation of photogenerated holes and reactive $•O2-$ radicals.
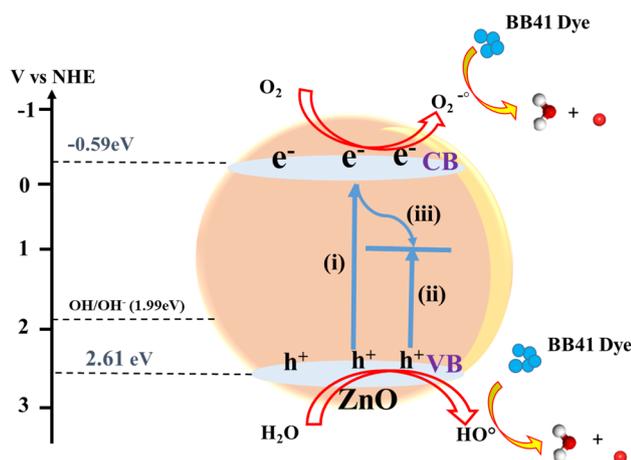
Fig. 12 Proposed schematic mechanism for the BB41 conversion using 20% cobalt doped ZnO photocatalyst

Comparison of photodegradation efficiency of organic molecules using modified ZnO in various literature works

A literature review of the subject of this article shows that several authors have studied the photocatalytic degradation of BB41 using various synthesized catalysts under both UV and visible illumination [79–84]; the results of these studies are reported in Table 7 in comparison with the present work under optimal operating conditions. To evaluate the degradation efficiency of BB41 under visible illumination, using the 20% cobalt doped ZnO photocatalyst synthesized by us, the results obtained in the present study have been compared (Table 7) with the results obtained by other authors. Thus, the variation in the degradation percentage and the necessary time of the mentioned treatments are affected by the catalyst used and the light nature. From the reported results, it could be concluded that the degradation efficiency of our optimized photocatalyst is very significant and competitive in terms of degradation percentage and the required time

especially that the initial concentration of BB41 in our study is higher than those of other studies.

Hence, 20% cobalt-doped ZnO synthesized in the current work could act as an excellent and effective photocatalyst with a considerable and highly satisfactory efficiency for the degradation of organic dyes compared to other photocatalysts used for various wastewater contaminants.

Conclusion

Cobalt-doped zinc oxide has been synthesized using the solution combustion method (SCM), then its characterization has been conducted using X-ray diffraction, X-ray fluorescence, DRS analysis, and BET surface area to examine its structural and textural characteristics. The results showed that cobalt dopant significantly decreased the bandgap from 3.18 to 2.67 eV, and increased the surface area from 3.4 to 7.7 m^2/g. Moreover, the experimental data show that the trend of theoretical calculation based on DFT indicated that the improvement in photocatalytic performance might be explained by adding new electrons in bandgap region of ZnO improving then the optical absorption properties of the ZnO and simplifying its band excitation and thus limits the recombination of electron–hole pairs. Furthermore, the mathematical model using the Box–Behnken design for BB41 degradation by cobalt doped ZnO could be a useful tool to predict the removal efficiency and optimize the operating conditions. Through using Box–Behnken design; it was found that:

- ANOVA showed a high correlation between actual and predicted values of the model.
- The optimization of factors for BB41 conversion indicated the following effect order: cobalt doping amount $(X_3) >$ pH $(X_1) >$ [BB41] (X_2).
- The optimum conditions: cobalt doping amount = 20%, pH = 11, and [BB41] = 26 ppm allowed to reach the max-

Table 7 Comparison of photodegradation efficiency of BB41 using different catalysts in various literature works

Catalyst	BB41 initial concentration (ppm)	Irradiation source	Time (min)	Degradation (%)	References
Cobalt (20%) doped ZnO	26	Visible light	120	100	Present work
$Bi_{12}NiO_{19}$	15	Visible light	180	98	[79]
TiO_2/palygorskite	12	UV light	70	90	[80]
Cu_2ZnSnS_4	12 ppm	Visible light	180	97.5	[81]
Sb_2S_3-TiO_2-SiO_2/TiO_2 nanotube arrays	10	Visible light	480	95	[82]
ZnO	20	UV light	180	72.56	[83]
10% Ce–TiO_2 films	12	Visible light	180	98	[84]

imum conversion of (100%) with a high value of TOC and COD within 120 min.

In conclusion, our research clearly demonstrates that the combined use of synthesis and characterization techniques accompanied by mathematical optimization methods allows us to obtain a ZnO catalyst doped with an optimal cobalt content (20%), which can be used as a photocatalyst for the degradation of BB41 more efficiently than those reported by other authors.

References

1. M. Zouheir et al., Nano Futur. **5**, 025004 (2021)
2. A. Hsini et al., J. Colloid Interface Sci. **585**, 560–573 (2021)
3. A. Dra et al., Sci. World J. **2020**, 8 (2020)
4. A. Thiam et al., J. Chem. **2020**, 14 (2020)
5. A. Dra et al., Sci. World J. **2020**, 4815767 (2020)
6. Y. Jiang, Y. Sun, H. Liu, F. Zhu, H. Yin, Dye. Pigment. **78**, 77–83 (2008)
7. L.E. Fragaa, M.V.B. Zanonia, Eclet. Quim. **34**, 27–36 (2009)
8. L.O. Pereira, R.V. Lelo, G.C.M. Coelho, F. Magalhães, J. Iran. Chem. Soc. **16**, 2281–2289 (2019)
9. S. Boudiaf et al., J. Environ. Chem. Eng. **9**, 105572 (2021)
10. M. Karimi-Nazarabad, E.K. Goharshadi, R. Mehrkhah, M. Davardoostmanesh, Sep. Purif. Technol. **279**, 119788 (2021)
11. M. Yousefi, H. Eshghi, M. Karimi-Nazarabad, A. Farhadipour, New J. Chem. **44**, 20470–20478 (2020)
12. M. Karimi-Nazarabad, H. Ahmadzadeh, E.K. Goharshadi, Sol. Energy. **227**, 426–437 (2021)
13. O.F.S. Khasawneh et al., J. Environ. Chem. Eng. **9**, 104921 (2021)
14. S. Feng, F. Li, J. Environ. Chem. Eng. **9**, 105488 (2021)
15. I. Mimouni et al., Environ. Sci. Pollut. Res. (2021). https://doi.org/10.1007/s11356-021-16146-w
16. O. Assila et al., J. Chem. **2020**, 1–13 (2020)
17. N. Davari, M. Farhadian, A.R.S. Nazar, M. Homayoonfal, J. Environ. Chem. Eng. **5**, 5707–5720 (2017)
18. T. Leshuk et al., ACS Appl. Mater. Interfaces. **5**, 1892–1895 (2013)
19. N. Chi, T. Mai, T. Thi, T. Van, R. Juang, Sep. Purif. Technol. (2020). https://doi.org/10.1016/j.seppur.2019.115962
20. R. Djellabi, L. Zhang, B. Yang, M.R. Haider, X. Zhao, Sep. Purif. Technol. **229**, 115830 (2019)
21. K. Priyanka, N. Remya, M. Behera, Sep. Purif. Technol. **251**, 117319 (2020)
22. H.S. Alanazi, N. Ahmad, F.A. Alharthi, RSC Adv. **11**, 10194–10202 (2021)
23. Z. Mirzaeifard, Z. Shariatinia, M. Jourshabani, S.M. Rezaei Darvishi, Ind. Eng. Chem. Res. **59**, 15894–15911 (2020)
24. K. Tanji et al., Catal. Today. In Press, 1–11 (2020).
25. K. Tanji et al., Chemosphere **241**, 125009 (2020)
26. M. Miyauchi, A. Nakajima, T. Watanabe, K. Hashimoto, Chem. Mater. **14**, 2812–2816 (2002)
27. S. Mozia et al., Appl. Catal. B Environ. **55**, 195–200 (2005)
28. U. Altinbaş, V. Eroğlu, I. Öztürk, Water Sci. Technol. **40**, 269–274 (1999)
29. K. Tanji et al., J. Photochem. Photobiol. A Chem. **382**, 111877 (2019)
30. M. Zouhier et al., J. Photochem. Photobiol. A Chem. **390**, 112305 (2020)
31. X. Ren et al., Sep. Purif. Technol. **270**, 118797 (2021)
32. Q. Wu, Y. Cui, L. Yang, G. Zhang, D. Gao, Sep. Purif. Technol. **142**, 168–175 (2015)
33. B. Dindar, A.C. Güler, A.C. Guler, Environ. Nanotechnol. Monit. Manag. **10**, 457–466 (2018)
34. W. Vallejo et al., Catalysts **10**, 528 (2020)
35. Y. Naciri et al., J. Colloid Interface Sci. **572**, 269–280 (2020)
36. Y. Lu et al., Nano Res. **4**, 1144–1152 (2011)
37. M.S. Hamdy et al., J. Nanostructure Chem. **11**, 147–163 (2020)
38. S. Lanfredi, M.A.L. Nobre, P.S. Poon, J. Matos, Molecules **25**, 96 (2020)
39. B. Ihssane et al., Acta Chromatogr. **23**, 41–57 (2011)
40. M.S. Shalaby, H. Abdallah, R. Chetty, M. Kumar, A.M. Shaban, Nano-Struct. Nano-Objects **19**, 100342 (2019)
41. I. Khouni, B. Marrot, R. Ben Amar, Chem. Eng. J. **156**, 121–133 (2010)
42. P. Giannozzi et al., J. Phys. Condens. Matter. **21**, 395502 (2009)
43. P. Giannozzi *et al.*, J. Phys. Condens. Matter. **29**, 465901 (2017).
44. J.P. Perdew, K. Burke, M. Ernzerhof, Phys. Rev. Lett. **77**, 3865–3868 (1996)
45. H.J. Lee, B.S. Kim, C.R. Cho, S.Y. Jeong, Phys. Status Solidi Basic Res. **241**, 1533–1536 (2004)
46. R. Elilarassi, G. Chandrasekaran, J. Mater. Sci. Mater. Electron. **24**, 96–105 (2013)
47. S. Kalpana, S.S. Krishnan, T.S. Senthil, S.V. Elangovan, J. Ovonic Res. **13**, 263–269 (2017)
48. K. Ravichandran et al., Powder Technol. **274**, 250–257 (2015)
49. G. Vijayaprasath, R. Murugan, T. Mahalingam, G. Ravi, J. Mater. Sci. Mater. Electron. **26**, 7205–7213 (2015)
50. N. Pushpa, M.K. Kokila, J. Lumin. **190**, 100–107 (2017)
51. M. Ivill et al., New J. Phys. **10**, 065002 (2008)
52. S.K. Mandal, A.K. Das, T.K. Nath, D. Karmakar, Appl. Phys. Lett. **89**, 1–4 (2006)
53. S.D. Birajdar, P.P. Khirade, V.R. Bhagwat, A.V. Humbe, K.M. Jadhav, J. Alloys Compd. **683**, 513–526 (2016)
54. S.D. Birajdar, P.P. Khirade, T.S. Saraf, R.C. Alange, K.M. Jadhav, J. Alloys Compd. **691**, 355–363 (2017)
55. E. Baeissa, Front. Nanosci. Nanotechnol. **2**, 1–5 (2016)
56. L. Roza, Y. Febrianti, S. Iwan, V. Fauzia, Surf. Interfaces **18**, 100435 (2020)
57. Z.N. Kayani, I. Shah, S. Riaz, S. Naseem, J. Mater. Sci. Mater. Electron. **28**, 5953–5961 (2017)
58. R. López, R. Gómez, J. Sol Gel Sci. Technol. **61**, 1–7 (2012)
59. H.A. Ahsaine et al., Chem. Select **3**, 7778–7791 (2018)
60. B.M. Rajbongshi, S.K. Samdarshi, Appl. Catal. B Environ. **144**, 435–441 (2014)
61. O. Gürbüz, S. Güner, Ö. Büyükbakkal, S. Çalişkan, J. Magn. Magn. Mater. **373**, 90–95 (2015)
62. P.R. Chithira, T. Theresa John, J. Magn. Magn. Mater. **496**, 165928 (2020)
63. M.V. Lopez-Ramon, F. Stoeckli, C. Moreno-Castilla, F. Carrasco-Marin, Carbon N. Y. **37**, 1215–1221 (1999)
64. S. Nam, H. Cho, J. Han, N. Her, J. Yoon, Process Saf. Environ. Prot. **113**, 10–21 (2018)
65. S. Sohrabi, F. Akhlaghian, Process Saf. Environ. Prot. **99**, 120–128 (2015)
66. A. Loqman, B. El Bali, J. Lützenkirchen, P.G. Weidler, A. Kherbeche, Appl. Water Sci. **7**, 3649–3660 (2017)
67. B. Samet, T. Mnif, M. Chaabouni, Cem. Concr. Compos. **29**, 741–749 (2007)

68. L. Elleuch et al., J. Hazard. Mater. (2020). https://doi.org/10.1016/j.jhazmat.2019.121119
69. A.M. Tayeb, M.A. Tony, E.K. Ismaeel, Appl. Water Sci. **9**, 43 (2019)
70. Q. Xiao, J. Zhang, C. Xiao, X. Tan, Mater. Sci. Eng. B Solid-State Mater. Adv. Technol. **142**, 121–125 (2007)
71. Y. Naciri et al., J. Environ. Chem. Eng. **6**, 1840–1847 (2018)
72. A.S. Manikandan, K.B. Renukadevi, K. Ravichandran, P.V. Rajkumar, K. Boubaker, J. Mater. Sci. Mater. Electron. **27**, 11890–11901 (2016)
73. R.M. Mohamed, D. McKinney, M.W. Kadi, I.A. Mkhalid, W. Sigmund, Ceram. Int. **42**, 2299–2305 (2016)
74. R. Marandi, M.E. Olya, A.A.M. Sharif, J. Saudi Chem. Soc. **18**, 317–326 (2014)
75. S. Sheik Mydeen, R. Raj Kumar, M. Kottaisamy, V.S. Vasantha, J. Saudi Chem. Soc. **24**, 393–406 (2020)
76. H.A. Kiwaan, T.M. Atwee, E.A. Azab, A.A. El-Bindary, J. Chin. Chem. Soc. **66**, 89–98 (2019)
77. H. Ait Ahsaine, Mater. Lett. **276**, 128221 (2020)
78. M. Mousavi, A. Habibi-yangjeh, M. Abitorabi, J. Colloid Interface Sci. **480**, 218–231 (2016)
79. B. Brahimi, H. Kenfoud, Y. Benrighi, O. Baaloudj, Photochemistry **1**, 319–329 (2021)
80. E. Stathatos, D. Papoulis, C.A. Aggelopoulos, D. Panagiotaras, A. Nikolopoulou, J. Hazard. Mater. **211–212**, 68–76 (2012)
81. A. Apostolopoulou, S. Mahajan, R. Sharma, E. Stathatos, J. Phys. Chem. Solids. **112**, 37–42 (2018)
82. M. Karimi-Shamsabadi, M. Behpour, Int. J. Hydrogen Energy. **46**, 26989–27013 (2021)
83. N.M. Mahmoodi, S. Keshavarzi, M. Ghezelbash, J. Environ. Chem. Eng. **5**, 3684–3689 (2017)
84. A. Rapsomanikis, A. Apostolopoulou, E. Stathatos, P. Lianos, J. Photochem. Photobiol. A Chem. **280**, 46–53 (2014)